Anisotropic optical properties of highly doped rutile SnO_2: Valence band contributions to the Burstein-Moss shift

Martin Feneberg, Christian Lidig, Mark E. White, Min Y. Tsai, James S. Speck, Oliver Bierwagen, Zbigniew Galazka, and Rüdiger Goldhahn

Citation: APL Materials **7**, 022508 (2019); doi: 10.1063/1.5054351
View online: https://doi.org/10.1063/1.5054351
View Table of Contents: http://aip.scitation.org/toc/apm/7/2
Published by the American Institute of Physics

Anisotropic optical properties of highly doped rutile SnO_2: Valence band contributions to the Burstein-Moss shift

Cite as: APL Mater. 7, 022508 (2019); doi: 10.1063/1.5054351
Submitted: 31 August 2018 • Accepted: 26 September 2018 •
Published Online: 13 December 2018

Martin Feneberg,[1,a] Christian Lidig,[1] Mark E. White,[2] Min Y. Tsai,[3] James S. Speck,[2] Oliver Bierwagen,[2,4] Zbigniew Galazka,[5] and Rüdiger Goldhahn[1]

AFFILIATIONS

[1] Institut für Physik, Otto-von-Guericke-Universität Magdeburg, Universitätsplatz 2, 39106 Magdeburg, Germany
[2] Materials Department, University of California, Santa Barbara, California 93106, USA
[3] Department of Electrical and Computer Engineering, University of California, Santa Barbara, California 93106, USA
[4] Paul Drude Institut für Festkörperelektronik, Hausvogteiplatz 5-7, 10117 Berlin, Germany
[5] Leibniz-Institut für Kristallzüchtung, Max-Born-Straße 2, 12489 Berlin, Germany

[a] Electronic mail: martin.feneberg@ovgu.de

ABSTRACT

The interband absorption of the transparent conducting semiconductor rutile stannic oxide (SnO_2) is investigated as a function of increasing free electron concentration. The anisotropic dielectric functions of SnO_2:Sb are determined by spectroscopic ellipsometry. The onsets of strong interband absorption found at different positions shift to higher photon energies with increasing free carrier concentration. For the electric field vector parallel to the optic axis, a low energy shoulder increases in prominence with increasing free electron concentration. We analyze the influence of different many-body effects and can model the behavior by taking into account bandgap renormalization and the Burstein-Moss effect. The latter consists of contributions from the conduction and the valence bands which can be distinguished because the nonparabolic conduction band dispersion of SnO_2 is known already with high accuracy. The possible originsof the shoulder are discussed. The most likely mechanism is identified to be interband transitions at $|k| > 0$ from a dipole forbidden valence band.

Tin-oxide is one of the two binary end points of ITO (indium tin oxide), currently one of the most frequently used materials for transparent contacts and electronics.[1,2] Usually, ITO is considered to be heavily Sn doped or alloyed In_2O_3 in its amorphous or polycrystalline form. To understand the optoelectronic properties of ITO and related materials better, many studies have been performed not only on ITO itself[3] but also on In_2O_3 in crystalline form.[4] However, tin-oxides are transparent conductive oxides in their own right and they are already successfully commercialized, e.g., in CdTe thin film solar cells[5] or as low emissivity layers on architectural glasses.[6] Furthermore, their usage is discussed, for example, in emerging perovskite solar cell materials.[7] Here, we concentrate on rutile SnO_2. It can be readily doped, e.g., by antimony (Sb) for n-type conductance and has a direct dipole forbidden bandgap in the ultraviolet. Furthermore, there is recent interest for possible applications of SnO_2 in sensor devices and catalysis,[8,9] spintronics,[10] and for usage in ransparent electronics.[11,12]

However, there is a lack of systematic experimental studies about the optical properties of crystalline rutile SnO_2 as a function of free carrier concentration in the literature. Most available studies deal with samples obtained by growth methods like the sol-gel method,[13] sputtering,[14] and spray pyrolysis.[15–17]

By contrast, this study provides high-quality optical data of single-crystalline SnO_2 samples with different free electron concentrations. We interpret the data from a semiconductor point of view and therefore link optical properties to the band structure of SnO_2. We employ state-of-the-art spectroscopic ellipsometry on a bulk SnO_2 crystal and high-quality molecular beam epitaxy grown thin films doped with antimony. The dielectric functions from the visible to the ultraviolet are obtained and analyzed. The electron concentration manifests itself in the optical spectra via many-body effects which are discussed in detail.

As a reference sample, a bulk SnO_2 sample grown at Leibniz-Institut für Kristallzüchtung (Berlin, Germany) by physical vapor transport with the (110) surface was used. Hall effect measurements yield an electron concentration of 7.4×10^{17} cm^{-3} and a mobility of μ = 207 cm^2 V^{-1} s^{-1}. Further details about growth and characteristics of this sample can be found elsewhere.[18] Six rutile SnO_2 thin film samples with (101) orientation with varying electron concentration were grown on $(01\bar{1}2)$ Al_2O_3 by plasma-assisted molecular beam epitaxy.[19,20] One sample was unintentionally doped ($n = 5.6 \times 10^{17}$ cm^{-3}), the other five layers were grown on top of such unintentionally doped templates and doped by different amounts of antimony. The resulting electron concentrations between 3.4×10^{18} and 2.6×10^{20} cm^{-3} were determined by Hall effect measurements in van-der-Pauw geometry. The thin-film samples have been investigated in the infrared spectral range earlier.[21] Key results to be used in this study include an increase of both effective electron masses $m_\perp^*$ and $m_\parallel^*$ with increasing free carrier concentration, however to a different extent. Thus, the conduction band dispersion of the anisotropic and non-parabolic conduction band of rutile SnO_2 is already known. Very recently, the anisotropy was verified independently by Hall effect measurements for bulk crystals with $n \approx 10^{18}$ cm^{-3}.[22] This anisotropy is increasing with increasing carrier concentration.[21] Dielectric limits are determined to be $\varepsilon_{\infty,\perp} = 3.70$ and $\varepsilon_{\infty,\parallel} = 3.90$.[21] Some important properties of the samples are tabulated in Table I.

Generalized spectroscopic ellipsometry[23] was performed on all samples in the photon energy range from 0.5 to 6.5 eV for at least three angles of incidence (θ = 60°, 67°, 74°). To access both the ordinary (electric field vector perpendicular to [001], $\mathbf{E}\perp\mathbf{c}$) and the extraordinary (electric field vector parallel to [001], $\mathbf{E}\parallel\mathbf{c}$) dielectric functions, each sample was measured twice, once with the optic axis of SnO_2 parallel to the plane of incidence and once rotated by 90° where [010] is parallel to the plane of incidence. The ratios of the complex reflection coefficients measured by generalized spectroscopic ellipsometry r_{pp}/r_{ss}, r_{ps}/r_{pp}, and r_{sp}/r_{ss} for both sample orientations are analyzed in a coupled multilayer model considering the Al_2O_3 substrate and the unintentionally doped SnO_2 template for samples A-F, the doped SnO_2 film or bulk crystal, and a surface layer accounting for roughness and possible electron accumulation layers for all samples. Such electron accumulation layers are expected to be <5 nm in thickness[24] which cannot be resolved sensitively individually in ellipsometry. The experimental technique of generalized spectroscopic ellipsometry is used to derive the optical properties of all samples in crystal coordinates. Therefore our results do not depend on the sample surface orientation.

The experimental data from the bulk SnO_2 sample are analyzed first. Ellipsometric parameters Ψ and Δ are shown for both sample orientations in Fig. 1 together with the respective point-by-point fits. The agreement of fits and experiment is close to perfect for high photon energies, while for lower energies small deviations can be observed. These deviations are attributed to backside reflections from the double-side polished SnO_2 bulk crystal which are not part of our optical model. Therefore, the photon energy of 3.5 eV where the deviations vanish is identified with the dipole forbidden bandgap energy of rutile SnO_2[27–30] because for higher photon energies a small but finite absorption is present in the material which attenuates the influence of the backside strongly.

Figure 2 shows the point-by-point fitted dielectric functions for electric field polarization perpendicular (ordinary DF) and parallel (extraordinary DF) to the optic axis obtained from the fits shown in Fig. 1. Additionally, the imaginary parts of the dielectric functions were fitted by Elliott's model[26] which are also shown in Fig. 2. Elliott's model for rutile SnO_2 consists for the ordinary dielectric function of a sum of three contributions

$$\varepsilon_{2,\perp} = \varepsilon_{2,\perp}^{X} + \varepsilon_{2,\perp}^{G} + \varepsilon_{2,\perp}^{D}, \quad (1)$$

TABLE I. Summary of the samples investigated: Hall carrier concentration n_{Hall}, Hall mobility μ_{Hall}, effective electron masses for the orientations perpendicular ($m_\perp^*$) and parallel ($m_\parallel^*$) to the optic axis.[21]

	Orientation	Dopant	n_{Hall} (cm^{-3})	μ_{Hall} (cm^2 V^{-1} s^{-1})	$m_\perp^*$ (m_0)	$m_\parallel^*$ (m_0)
bulk	(110)		7.4×10^{17}	207		
A	(101)		5.6×10^{17}	95		
B	(101)	Sb	3.4×10^{18}	85		
C	(101)	Sb	1.6×10^{19}	62	0.22 ± 0.03	0.20 ± 0.02
D	(101)	Sb	2.6×10^{19}	61	0.26 ± 0.02	0.20 ± 0.02
E	(101)	Sb	1.3×10^{20}	47	0.31 ± 0.03	0.22 ± 0.03
F	(101)	Sb	2.6×10^{20}	35	0.39 ± 0.04	0.26 ± 0.04

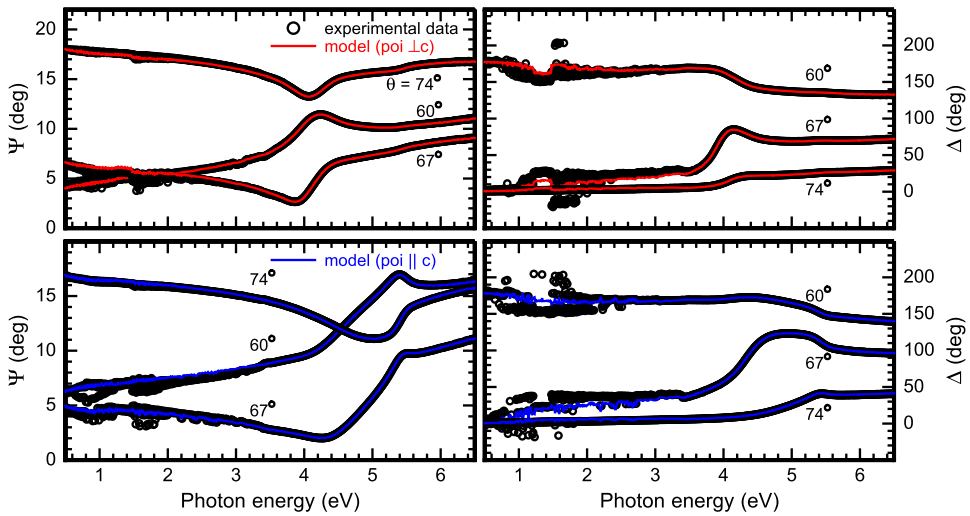

FIG. 1. Ellipsometric angles Ψ (left) and Δ (right) from the bulk sample. The plane of incidence (poi) is perpendicular to [001] (*c*) in the top row and parallel to *c* in the bottom row. Shown are experimental data points (symbols) and point-by-point fits (continuous curves) for three angles of incidence θ. Agreement of the fit and the experimental data is perfect for photon energies above 3.5 eV.

where the different contributions are discrete excitons (ε_2^X) with the exciton binding energy E_B^X and the broadening parameter γ, an exciton continuum (ε_2^G) above the direct allowed bandgap E_G with broadening parameter γ^G, and a contribution from higher *k* states (ε_2^D) from the direct dipole forbidden fundamental gap E^D,

$$\varepsilon_2^X = \frac{C^X}{(\hbar\omega)^2\gamma}\exp\left(-\frac{(\hbar\omega - E_G + E_B^X)^2}{\gamma^2}\right), \tag{2}$$

$$\varepsilon_2^G = \frac{C^G}{(\hbar\omega)^2}\frac{1+\mathrm{erf}\left(\frac{\hbar\omega - E_G}{\gamma^G}\right)}{1-\exp\left(-2\pi\sqrt{\frac{E_B^X}{|\hbar\omega - E_G|}}\right)}, \tag{3}$$

$$\varepsilon_2^D = C^D\left(\hbar\omega - E^D\right)^{3/2}\Theta\left(\hbar\omega - E^D\right). \tag{4}$$

Here C^X, C^G, and C^D are amplitude parameters and Θ is the Heaviside step function. The dipole allowed bandgap is at 4.29 eV, and the exciton binding energy is found to be 43 meV.

For the extraordinary dielectric function, four contributions are needed

$$\varepsilon_{2,\parallel} = \varepsilon_{2,\parallel}^X + \varepsilon_{2,\parallel}^{G1} + \varepsilon_{2,\parallel}^{G2} + \varepsilon_{2,\parallel}^D, \tag{5}$$

with the same mathematical expression as above [Eqs. (2)–(4)]. However, two independent exciton continua are required here (ε_2^{G1} and ε_2^{G2}). We find allowed bandgaps of 4.80 and 5.34 eV and an exciton binding energy of 59 meV.

In the next step, the unintentionally doped sample A is analyzed. The results from this step enter the analysis of the doped films as the template material.

The ordinary and the extraordinary dielectric functions are shown in Fig. 3. The direct allowed bandgaps E^G are found at 4.36 eV for the ordinary and 4.69 and 5.36 eV for the extraordinary dielectric function. These results are close to that from the bulk sample. We repeat this analysis for the doped samples. In Fig. 4, the point-by-point fitted dielectric functions of all thin film samples (A-F) are collected. It can be clearly seen that for both the ordinary and the extraordinary dielectric functions systematic changes in the dielectric functions are found. At low photon energies, an increase in ε_2 and a decrease in ε_1 are obvious for increasing free electron concentrations in both dielectric functions. This stems from the free carrier contribution to the dielectric function and can be described by the Drude model, more details are published in Ref. 25. In the transparency spectral range between ≈1.5 and 4 eV, the real parts of the dielectric functions decrease

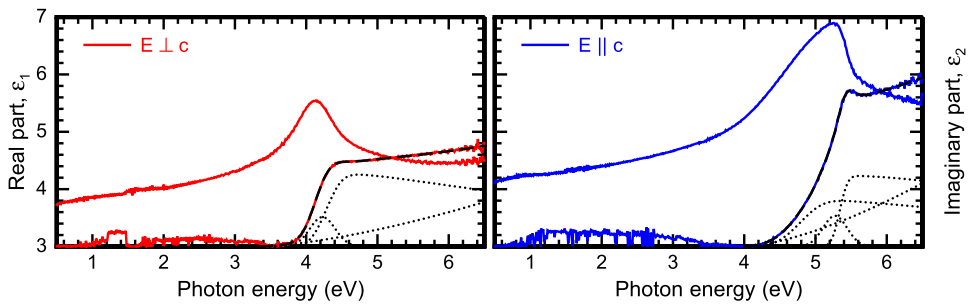

FIG. 2. Ordinary (left) and extraordinary (right) complex dielectric functions of the bulk sample. The point-by-point fitted ordinary dielectric functions are shown as continuous curves. Black dashed curves represent the fit by Elliott's model to the imaginary parts. The single components of the fits are shown as dotted curves.

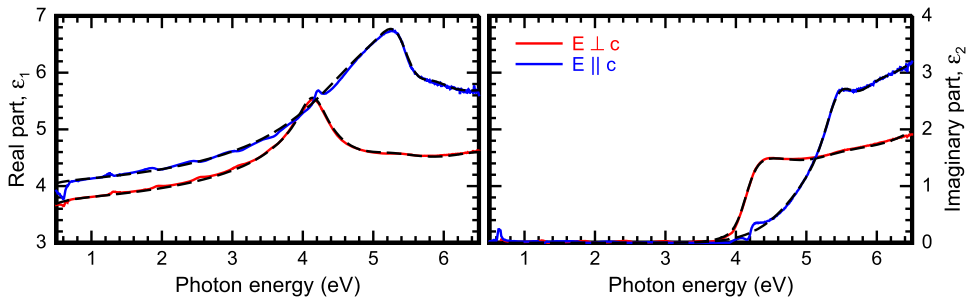

FIG. 3. Dielectric functions for the unintentionally doped sample A. The point-by-point fitted ordinary dielectric function is shown in red, the extraordinary one in blue. Black dashed curves represent the dielectric function from the parametric model.

for increasing n which is due to the combination of Drude contribution and the blue-shift of the bandgap energy with increasing n as described for the example of bixbyite In_2O_3 in detail elsewhere.[4] Due to the better signal-to-noise ratio, this effect is better seen in **E**⊥**c** than in **E**∥**c**. The effective blue-shift of the absorption onset finally is visible in both dielectric functions. However, in the imaginary part ε_2 of the extraordinary dielectric function a low energy shoulder develops to be more prominent with increasing free electron concentration (between 4 and 5 eV). In the real part ε_1, a broad peak-like feature is found at the same energy position in agreement with Kramers-Kronig consistency. In the model [Eqs. (1)–(5)], the additional feature is accounted for by the additional exciton continuum and will be discussed in more detail below.

From work decades ago,[27–30] it is known that the fundamental bandgap of rutile SnO_2 at 3.56 eV is dipole forbidden. In the dielectric function, we therefore observe transitions from lower valence bands into the conduction band which are found at higher photon energies than 3.56 eV. The polarization resolved two onsets of strong absorption were assigned to be transitions from valence bands having Γ_5^- (**E**⊥**c**) and Γ_2^- (**E**∥**c**) symmetries.[31] The observed blue-shifts of both fundamental absorption onsets are governed by the many-body effects bandgap renormalization and Burstein-Moss shifts. Because the conduction band dispersion is already fully known from infrared studies,[21] we can learn about the valence band contributions to the Burstein-Moss shifts from the energy shifts of the interband absorption onsets.

Similar to the case of In_2O_3, we are dealing here with a non-parabolic conduction band; i.e., the effective electron mass is not constant.[4] However, rutile SnO_2 is anisotropic,[21,22] like e.g., wurtzite GaN.[32] Thus, we have to use an anisotropic *and* non-parabolic model to describe the interband absorption shifts in SnO_2. We use the empiric non-parabolic conduction band dispersion proposed by Pisarkiewicz originally for rutile SnO_2,[33]

$$\frac{\hbar^2 k^2}{2m^*} = E + CE^2. \tag{6}$$

This dispersion relation can be used to describe the carrier dependent effective electron masses as

$$m_j^*(n) = m_{0,j}^* \sqrt{1 + 2C_j \frac{\hbar^2}{m_{0,j}^*}(3\pi^2 n)^{2/3}}, \tag{7}$$

with $j = \perp, \parallel$. From fitting Eq. (7) to the experimentally obtained effective masses,[21] we obtain the parameters $m_{0,\perp}^* = 0.205 m_0$, $m_{0,\parallel}^* = 0.183 m_0$, $C_\perp = 0.73\ \mathrm{eV}^{-1}$, and $C_\parallel = 0.33\ \mathrm{eV}^{-1}$. Values for

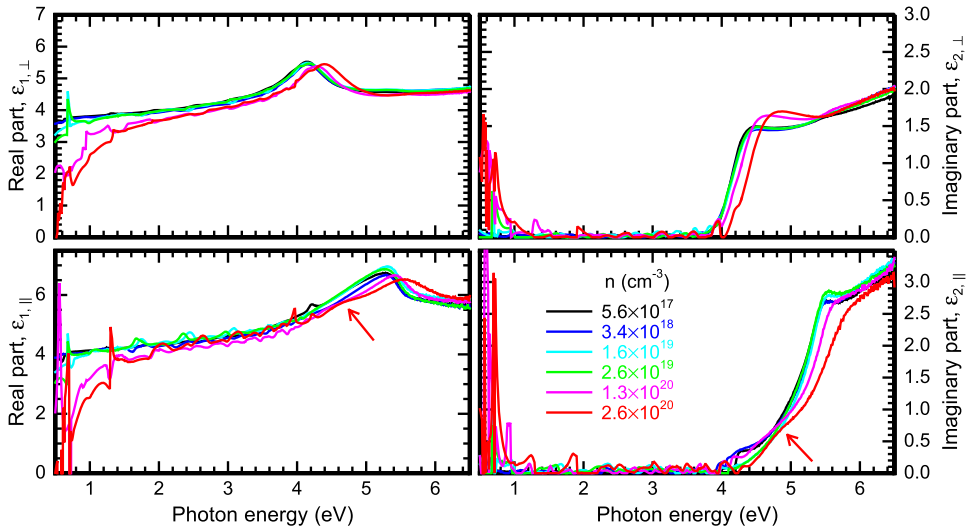

FIG. 4. Point-by-point fitted dielectric functions for all six thin film samples. The ordinary dielectric functions are shown in the top panels, the extraordinary ones in the bottom panels. Real parts are drawn on the left side, imaginary parts on the right side. The additional feature in the extraordinary dielectric function is marked by arrows for the sample with the highest electron concentration (F).

the same parameters were also calculated theoretically,[34] and the results are in perfect agreement with our experiment with the notable exception of $C_{\perp,theo.} = 0.45\ eV^{-1}$.

However, in Eq. (6) the anisotropy is not accounted for. Therefore, we replace the momentum k, the effective electron mass m_0^*, and the anisotropy parameter C in Eq. (6) by their counterparts averaged over the density of states ($k_D = \sqrt[3]{k_\perp^2 k_\parallel}$, $m_{0,D}^* = \sqrt[3]{m_{0,\perp}^{*\,2} m_{0,\parallel}^*} = 0.197 m_0$, and $C_D = \sqrt[3]{C_\perp^2 C_\parallel} = 0.56\ eV^{-1}$). The Fermi energy only depends on these averaged parameters and the free electron concentration n. It can be approximated as

$$E_F(n) = \frac{1}{2C_D}\left(\sqrt{1 + 2C_D \frac{\hbar^2}{m_{0,D}^*}(3\pi^2 n)^{2/3}} - 1\right). \quad (8)$$

From here, we calculate the anisotropic Fermi wavevectors $k_{F,\perp}$ and $k_{F,\parallel}$ by

$$k_{F,j} = \frac{1}{\hbar}\sqrt{2 m_j^*(n) E_F(n)}. \quad (9)$$

To describe bandgap renormalization, we use the same approach as described in Ref. 4 by inserting the density of states averaged parameters. The Burstein-Moss shift consists of contributions from the conduction and the valence bands. The Fermi energy as given in Eq. (8) is measured from the conduction band minimum and thus exactly equals the contribution from the conduction band to the Burstein-Moss shift. It is independent of the optical polarization direction. The valence bands are for simplicity approximated by parabolic dispersion relations as

$$E_{j,l}(k) = \frac{\hbar^2 k_j^2}{2 m_{j,l}^*}. \quad (10)$$

Here, $l = 1, 2$ for $j = \parallel$ and $l = 1$ for $j = \perp$. The effective hole masses for the valence bands at the Γ-point of the Brillouin zone were calculated in Ref. 31 to be $m_\perp^* = 1.21 m_0$ and $m_\parallel^* = 1.47 m_0$, respectively. We use these effective hole masses for simplicity for $l = 1$ and $l = 2$. The experimentally obtained transition energies and the modeled dependence using these parameters are compared in Fig. 5. The relatively large spacing of the valence bands makes the decomposition of the different contributions easier than, for example, in wurtzite GaN.[35]

The agreement between the model curves describing the combined effects of bandgap renormalization and Burstein-Moss shifts and the experimentally determined bandgap energies is very good despite the fact that the effective hole masses reported in Ref. 31 are explicitly given for the topmost valence band expressing Γ_3^+ symmetry which does not contribute to observable interband absorption. However, close inspection of Fig. 5 reveals that a slightly smaller effective hole mass for the valence bands contributing to absorption in $\mathbf{E}\parallel\mathbf{c}$ might also be in order.

The transition occurring for $\mathbf{E}\perp\mathbf{c}$ is unambiguously identified as an interband transition involving the Γ_5^- valence band and the Γ_1^+ conduction band. By contrast, for $\mathbf{E}\parallel\mathbf{c}$ we find two different characteristic energies at 4.69 and 5.36 eV for $n \to 0$. The higher energy transition is clearly assigned to interband transitions involving the Γ_2^- valence band and the conduction band, the lower energy one however has not been identified unambiguously before. Because the corresponding signal increases in prominence for increasing free electron concentration, it can be assigned to different origins all related to free carriers directly or indirectly. Different possibilities are

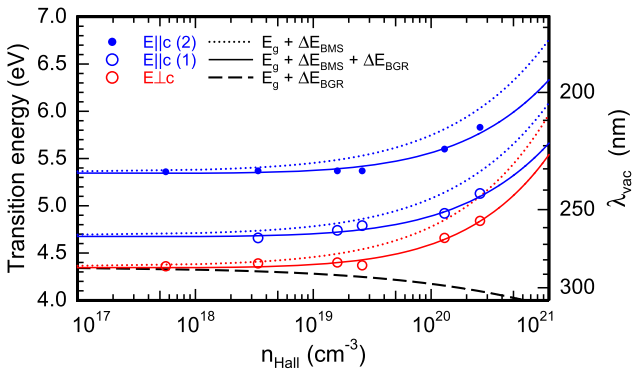

FIG. 5. Energies of the bandgaps for all observed transitions (symbols). The electron concentration dependent transition energies according to the model are given as curves. The dotted curves symbolize the Burstein-Moss shifts only, the dashed curve is the bandgap renormalization (only shown for the lowest energy transition for clarity), and continuous curves are the sums of both contributions.

- According to the classical Elliott theory of absorption in semiconductors taking Coulomb interaction into account,[26] a direct but dipole forbidden transition contributes for $k > 0$ to the interband absorption.
- Peelaers and colleagues proposed phonon assisted free carrier absorption to happen in doped SnO_2.[36,37] This process is basically an intra-conduction band absorption process.
- Ha *et al.* investigated the so-called second gap in SnO_2 theoretically.[38] This second gap is an interband transition from the lowest conduction band to the next higher energy conduction band.

All these models are schematically explained in Fig. 6. We will now discuss these models with respect to our experimental data (Fig. 4). This discussion is strongly dependent on the assumed band structure of rutile SnO_2, i.e., energy differences between certain bands and effective masses. We are using the band structure theoretically computed in Ref. 31 which has already been shown to provide a good agreement with experimental results in terms of dielectric functions over a large spectral range.[25]

Elliott's model for the top of the valence bands in SnO_2 is sketched in Figs. 6(a) and 6(b) for an increased free electron concentration. The lower energy valence band in Figs. 6(a) and 6(b) symbolizes the Γ_2^- valence band contributing to the onset of strong absorption for $\mathbf{E}\parallel\mathbf{c}$. By contrast, the higher one represents one of the dipole forbidden valence bands (for $\mathbf{E}\parallel\mathbf{c}$) with increasing optical dipole strength for increasing momentum [Eq. (4)]. This model has been successfully used to interpret absorption edges of SnO_2 earlier.[25] Testing of this model against our experimental results yields a possible

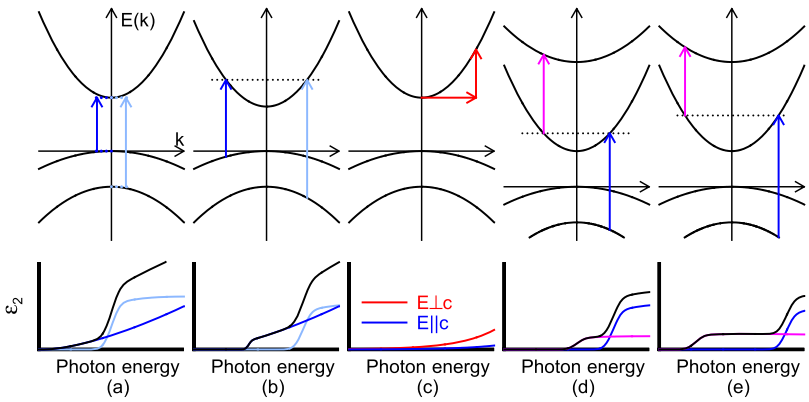

FIG. 6. Schematic band structure representations of different models to explain the observed second contribution for **E**||**c**. (a) and (b) Elliott's model taking into account a dipole forbidden transition at $k = 0$ which gains in transition strength for $|k| > 0$, the shown valence bands have Γ_5^+ and Γ_2^- symmetry from top to bottom, (c) phonon-assisted intra-conduction band absorption, (d) and (e) inter-conduction band transitions which are also called second gap transitions. Dotted horizontal lines represent Fermi energy levels, the higher the Fermi level, the higher the free electron concentration.

agreement: For increasing Fermi energy both transition energies are expected to shift to higher photon energies as observed because the electron effective mass is lower than the hole effective masses of the contributing bands. Inspection of the valence band structure at the Γ point of the Brillouin zone yields the Γ_5^+ valence band as a likely candidate for the dipole forbidden transition. Please note that this valence band is not identical to the topmost valence band which has Γ_3^+ symmetry and is included in our model by Eq. (4). Theory finds a distance of 0.78 eV between Γ_2^- and Γ_5^+ valence bands at $n = 0$.[31] Extrapolation of our experimental results to $n \to 0$ yields an experimental value of 0.67 eV. The energy difference between Γ_5^- and Γ_5^+ valence bands is theoretically predicted to be 0.39 eV while our experiment yields 0.33 eV. This model therefore is a viable explanation for the experimental results.

Figure 6(c) accounts for phonon-assisted intra-conduction band absorption which was investigated in detail by Peelaers *et al.*[36,37] by first-principles calculations. In these studies, the absorption cross section is reported which we converted to imaginary parts of the dielectric functions for this discussion. One of the results is that the amplitudes of the predicted ε_2 due to phonon-assisted intraband absorption are below 0.05 for the spectral range between ≈2 and 4.3 eV. Moreover, the ordinary contribution is predicted to be stronger than the extraordinary one which clearly contradicts our experimental findings where the observed effect is stronger for **E**||**c**. Therefore, we are confident that the here observed effect is not dominated by phonon-assisted intraband absorption.

The third possibility is put forward by Ha and colleagues and describes the so-called second gap.[38] The involved processes are schematically shown in Figs. 6(d) and 6(e) for increasing free-electron concentration, respectively. According to the band structure, the second conduction band has a larger effective mass than the fundamental conduction band or even a negative effective mass.[31] Therefore, increasing Fermi energies lead to decreasing photon energies for the absorption onset of the second gap. This holds true even when accounting for bandgap renormalization assuming that only the fundamental conduction band is down-shifted. The Burstein-Moss shift of the lowest conduction band alone is already larger than the bandgap renormalization. Thus, this model cannot explain our experimental results either and we are left with Elliott's theory considering a dipole forbidden transition.

The best model to explain our experimental findings is therefore the Elliott model as shown in Figs. 6(a) and 6(b). To describe the optical properties of rutile SnO_2, we have to take four valence bands into account: The topmost valence band with Γ_3^+ symmetry is dipole forbidden at $k = 0$. Its contribution for $|k| > 0$ is modeled by Eq. (4). For **E**⊥**c** we find allowed absorption from the valence band with Γ_5^- symmetry. For **E**||**c**, we have two contributions, one at lower photon energy from the Γ_5^+ valence band and a stronger one at higher photon energy from the Γ_2^- valence band. To differentiate the latter two is facilitated by the observation of their blue-shift with increasing free-electron concentration.

In summary, we experimentally investigated rutile SnO_2 thin films with different free-electron concentrations. Spectroscopic ellipsometry yields anisotropic dielectric functions ε. For **E**⊥**c**, we found a blue-shift of the absorption onset which is quantitatively explained by a combination of bandgap renormalization and Burstein-Moss shift. The Burstein-Moss shift for **E**⊥**c** is stronger than that for **E**||**c**. For the latter case, two characteristic contributions are found which both undergo a blue-shift. The higher energy absorption onset is identified with a dipole allowed interband transition; for the lower energy one, a transition from a different valence band with Γ_5^- symmetry is the best explanation.

We acknowledge funding by the Deutsche Forschungsgemeinschaft DFG in the framework of Major Research Instrumentation Program No. INST272/205-1. Part of this work was performed within the framework of GraFOx, a Leibniz-Science campus.

REFERENCES

[1] T. Minami, Semicond. Sci. Technol. **20**, S35 (2005).
[2] E. Fortunato, P. Barquinha, and R. Martins, Adv. Mater. **24**, 2945 (2012).
[3] I. Hamberg and C. G. Granqvist, J. Appl. Phys. **60**, R123 (1986).
[4] M. Feneberg, J. Nixdorf, C. Lidig, R. Goldhahn, Z. Galazka, O. Bierwagen, and J. S. Speck, Phys. Rev. B **93**, 045203 (2016); Erratum, **94**, 239905 (2016).

[5]A. Polman, M. Knight, E. C. Garnett, B. Ehrler, and W. C. Sinke, Science **352**, 307 (2016).
[6]C. Schaefer, G. Bräuer, and J. Szczyrbowski, Surf. Coat. Technol. **93**, 37 (1997).
[7]M. A. Green, A. Ho-Baillie, and H. J. Snaith, Nat. Photonics **8**, 506 (2014).
[8]M. Batzill and U. Diebold, Prog. Surf. Sci. **79**, 47 (2005).
[9]A. Tischner, T. Maier, C. Stepper, and A. Köck, Sens. Actuators, B **134**, 796 (2008).
[10]S. B. Ogale, R. J. Choudhary, J. P. Buban, S. E. Lofland, S. R. Shinde, S. N. Kale, V. N. Kulkarni, J. Higgins, C. Lanci, J. R. Simpson, N. D. Browning, S. Das Sarma, H. D. Drew, R. L. Greene, and T. Venkatesan, Phys. Rev. Lett. **91**, 077205 (2003).
[11]R. E. Presley, C. L. Munsee, C.-H. Park, D. Hong, J. F. Wager, and D. A. Keszler, J. Phys. D: Appl. Phys. **37**, 2810 (2004).
[12]M. Grundmann, F. Klüpfel, R. Karsthof, P. Schlupp, F.-L. Schein, D. Splith, C. Yang, S. Bitter, and H. von Wenckstern, J. Phys. D: Appl. Phys. **49**, 213001 (2016).
[13]C. Terrier, J. P. Chatelon, and J. A. Roger, Thin Solid Films **295**, 95 (1997).
[14]K. Suzuki and M. Mizuhashi, Thin Solid Films **97**, 119 (1982).
[15]J.-C. Manifacier, L. Szepessy, J. F. Bresse, M. Perotin, and R. Stuck, Mater. Res. Bull. **14**, 109 (1979); **14**, 163 (1979).
[16]E. Elangovan and K. Ramamurthi, Cryst. Res. Technol. **38**, 779 (2003).
[17]A. A. Yadav, E. U. Masumdar, A. V. Moholkar, M. Neumann-Spallart, K. Y. Rajpure, and C. H. Bhosale, J. Alloys Compd. **488**, 350 (2009).
[18]Z. Galazka, R. Uecker, D. Klimm, K. Irmscher, M. Pietsch, R. Schewski, M. Albrecht, A. Kwasniewski, S. Ganschow, D. Schulz, C. Guguschev, R. Bertram, M. Bickermann, and R. Fornari, Phys. Status Solidi A **211**, 66 (2014).
[19]M. E. White, M. Y. Tsai, F. Wu, and J. S. Speck, J. Vac. Sci. Technol., A **26**, 1300 (2008).
[20]M. E. White, O. Bierwagen, M. Y. Tsai, and J. S. Speck, J. Appl. Phys. **106**, 093704 (2009).
[21]M. Feneberg, C. Lidig, K. Lange, M. E. White, M. Y. Tsai, J. S. Speck, O. Bierwagen, and R. Goldhahn, Phys. Status Solidi A **211**, 82 (2014).
[22]O. Bierwagen and Z. Galazka, Appl. Phys. Lett. **112**, 092105 (2018).
[23]M. Schubert, B. Rheinländer, J. A. Woollam, B. Johs, and C. M. Herzinger, J. Opt. Soc. Am. A **13**, 875 (1996).
[24]S. K. Vasheghani Farahani, T. D. Veal, J. J. Mudd, D. O. Scanlon, G. W. Watson, O. Bierwagen, M. E. White, J. S. Speck, and C. F. McConville, Phys. Rev. B **90**, 155413 (2014).
[25]M. Feneberg, C. Lidig, K. Lange, R. Goldhahn, M. D. Neumann, N. Esser, O. Bierwagen, M. E. White, M. Y. Tsai, and J. S. Speck, Appl. Phys. Lett. **104**, 231106 (2014).
[26]R. J. Elliott, Phys. Rev. **108**, 1384 (1957).
[27]N. Nagasawa and S. Shionoya, Phys. Lett. **22**, 409 (1966).
[28]N. Nagasawa and S. Shionoya, Phys. Rev. Lett. **21**, 1070 (1968).
[29]V. T. Agekyan, Phys. Status Solidi A **43**, 11 (1977).
[30]D. Fröhlich, R. Kenklies, and R. Helbig, Phys. Rev. Lett. **41**, 1750 (1978).
[31]A. Schleife, J. B. Varley, F. Fuchs, C. Rödl, F. Bechstedt, P. Rinke, A. Janotti, and C. G. Van de Walle, Phys. Rev. B **83**, 035116 (2011).
[32]M. Feneberg, S. Osterburg, K. Lange, C. Lidig, B. Garke, R. Goldhahn, E. Richter, C. Netzel, M. D. Neumann, N. Esser, S. Fritze, H. Witte, J. Bläsing, A. Dadgar, and A. Krost, Phys. Rev. B **90**, 075203 (2014).
[33]T. Pisarkiewicz and A. Kolodziej, Phys. Status Solidi B **158**, K5 (1990).
[34]C. Rödl and A. Schleife, Phys. Status Solidi A **211**, 74 (2014).
[35]M. Feneberg, M. Winkler, K. Lange, M. Wieneke, H. Witte, A. Dadgar, and R. Goldhahn, Appl. Phys. Express **11**, 101001 (2018).
[36]H. Peelaers, E. Kioupakis, and C. G. Van de Walle, Appl. Phys. Lett. **100**, 011914 (2012).
[37]H. Peelaers, E. Kioupakis, and C. G. Van de Walle, Phys. Rev. B **92**, 235201 (2015).
[38]V.-A. Ha, D. Waroquiers, G.-M. Rignanese, and G. Hautier, Appl. Phys. Lett. **108**, 201902 (2016).